New alkaline-earth amidosulfates and their unexpected decomposition to S$_4$N$_4$†

Peter Gross,‡[a] Yue Zhang,[a] Lkhamsuren Bayarjargal,[b] Björn Winkler[b] and Henning A. Höppe ⓘ *[a]

The amidosulphates Mg(NH$_2$SO$_3$)$_2$·4H$_2$O ($P2_1/c$), Mg(NH$_2$SO$_3$)$_2$·3H$_2$O ($P\bar{1}$), Ca(NH$_2$SO$_3$)$_2$·4H$_2$O ($C2/c$), Ca(NH$_2$SO$_3$)$_2$·H$_2$O ($P2_12_12_1$), Sr(NH$_2$SO$_3$)$_2$·4H$_2$O ($C2/c$), Sr(NH$_2$SO$_3$)$_2$·H$_2$O ($P2_1/c$) and Ba(NH$_2$SO$_3$)$_2$ ($Pna2_1$) could be obtained as cm-sized crystals from aqueous solutions of the corresponding metal carbonates, hydroxides and amidosulphonic acid, respectively, by careful control of the crystallisation conditions. β-Sr(NH$_2$SO$_3$)$_2$ (Pc) and α-Sr(NH$_2$SO$_3$)$_2$ ($P2_1$) could be obtained by careful thermal dehydration of Sr(NH$_2$SO$_3$)$_2$·H$_2$O. Their crystal structures were determined by single-crystal XRD and revealed a rich structural diversity with a significant tendency to form non-centrosymmetric crystals. The compounds were characterised by powder XRD, FT-IR, Raman and UV/vis spectroscopy and thermogravimetry. Temperature programmed single-crystal XRD, powder XRD and Raman spectroscopy, as well as DFT calculations were employed to aid the interpretation of vibrational and thermal properties. For the first time, SHG measurements were performed on metal amidosulphates, revealing the SHG intensities of β-Sr(NH$_2$SO$_3$)$_2$ and Ba(NH$_2$SO$_3$)$_2$ that were comparable to quartz and KDP. Thermal decomposition was additionally studied by the preparation of reaction intermediates, serendipitously revealing the formation of S$_4$N$_4$ as the decomposition product. This unprecedented reaction represents the first sulphur nitride synthesis process that neither employs a sulphur halide nor elemental sulphur.

1.   Introduction

Silicate-analogous materials feature anionic tetrahedral building units, TX$_4$, and they still hide numerous secrets about their structures, exciting properties and the chemistry behind them. They behave structurally and chemically often like their respective silicate anions. During our research, we came across phosphates,[1–5] borophosphates,[6,7] and recently borosulphates.[8–11] Of course, also derivatives of such oxoanions are of interest,[12–14] and such a derivative of oxosulphates are amido-sulphates. Herein, we describe the syn-

thesis, crystallisation and crystal structures, as well as the thermal, vibrational and optical properties of alkaline earth amidosulphates. Their remarkable potential for nonlinear optical materials is highlighted by this first study reporting on the second harmonic generation of metal amidosulphates; moreover, their astonishing thermal decomposition to S$_4$N$_4$ is reported, opening a novel, unprecedented access to sulphur nitrides.

Amidosulphuric acid (also called sulphamic acid, amidosulphonic acid or sulphamidic acid) is a large-scale commodity chemical with a worldwide annual production of about 96 000 t. It is obtained from urea and oleum as a crystalline, nontoxic, air- and moisture-stable white powder.[15,16] Its main uses include the synthesis of cyclamates as sweeteners,[17] as reagents in wax[18] and paper industries,[19] as a flame retardant,[17] as a reagent for various medical applications,[20] for the synthesis of herbicides[17] and in the course of boiler scale removal (*i.e.* magnesium/calcium carbonates/phosphates with minor strontium and barium contents).[21] The latter suggests the formation and disposal of alkaline earth amidosulphates on an industrial scale—potentially wasting an unrecognised resource.

Though dibasic imidosulphate [NHSO$_3$]$^{2-}$ anions[22,23] and tribasic nitridosulphate [NSO$_3$]$^{3-}$ anions[24–26] have been occasionally encountered, most of the studies on the crystal

structures of the metal salts of amidosulphuric acid feature monobasic amidosulphate $[NH_2SO_3]^-$ anions. For monovalent ions, besides the double salts $MLi(NH_2SO_3)_2$ (M = K, Rb, and Cs),[27] amidosulphates of the alkali metal ions Li^+ to Cs^+,[28–37] the pseudo-alkali cations ammonium, Ag^+ and Tl^+ have been structurally characterised.[31,38–41] The crystal structures of amidosulphates containing the divalent cations Ba^{2+}, Ca^{2+}, Mn^{2+}, Ni^{2+}, Pb^{2+} and UO_2^{2+} have been determined.[42–45] Furthermore, some amidosulphate structures of trivalent rare-earth cations (La^{3+}, Pr^{3+}, Nd^{3+} and Sm^{3+}) have been described.[46–48]

The crystal chemistry of amidosulphates known so far reveals some interesting crystallographic properties, namely piezoelectricity,[31] polymorphism,[31,37,49–51] and a general tendency to form non-centrosymmetric structures.[30,32,36,40,48] Surprisingly, to the best of our knowledge, no second-harmonic generation measurement has been published on any metal amidosulphate compound as yet. Several studies on the thermal decomposition of metal amidosulphates suggested a quite complex decomposition pattern,[22,47,52] in parts involving condensation reactions to imidodisulphates, which is a first indication that such species might be suitable precursors to sulphur nitrides.

Sulphur nitrides are hitherto obtained by the reaction of highly reactive starting materials like sulphur halides and liquid ammonia, employing corresponding laboratory equipment and ensuring inert gas conditions as well as sometimes elaborate post-synthetic purification steps. Within our ongoing quest for promising optical materials,[2–6,10,53–55] we regularly employ cheap and easy-to-use urea-based precursors[56–59] for the synthesis of nitride materials. As typical waste products of boiler scale removal, both cheap and easy to handle under ambient conditions, we decided to study alkaline-earth amidosulphates with special emphasis on structure elucidation, vibrational spectroscopy, thermal degradation and NLO properties.

2 Experimental section

2.1 Synthesis

$Mg(NH_2SO_3)_2 \cdot 4H_2O$ (**1**), $Ca(NH_2SO_3)_2 \cdot 4H_2O$ (**3**), $Sr(NH_2SO_3)_2 \cdot 4H_2O$ (**5**) and $Ba(NH_2SO_3)_2$ (**9**) were synthesised by a simple acid–base reaction of 2 mmol $Mg(OH)_2$ or the respective metal carbonate MCO_3 (M = Ca, Sr, and Ba) with 4 mmol amidosulphonic acid dissolved in 3 ml of demineralised water. The resulting solution was heated using a hot plate below the boiling point under stirring until a clear solution was obtained. It is then removed from the hot plate and allowed to cool to room temperature. The product was subsequently crystallised *via* slow evaporation at about 30 °C over several days in a beaker covered by perforated parafilm. Depending on the amount and sizes of holes in the parafilm as well as the size of the employed beaker, crystals of a diameter of several centimetres could be obtained (Fig. S74†) in quantitative yields. $Mg(NH_2SO_3)_2 \cdot 3H_2O$ (**2**), $Ca(NH_2SO_3)_2 \cdot H_2O$ (**4**) and $Sr(NH_2SO_3)_2 \cdot H_2O$ (**6**) were synthesised by leaving samples of the

respective tetrahydrates **1**, **3** and **5** after initial crystallisation from solution in the same beaker for several more days, until all visible liquid had been evaporated. β-$Sr(NH_2SO_3)_2$ (**7**) can be obtained if the monohydrate **6** is further kept in the beaker and slowly dehydrated. If **6** is directly exposed to dry air by removing the parafilm completely, the resulting crystallite size is significantly smaller and not sufficient for single-crystal XRD. α-$Sr(NH_2SO_3)_2$ (**8**) was obtained by drying the tetrahydrate **5** at about 100° in a compartment dryer for about 8 h and transferring the obtained powder into a soda-lime glass ampoule, which is subsequently torch sealed. The ampoule was heated to 250 °C at a heating rate of 10 K h^{-1} in a chamber furnace in an upright position, held at that temperature for 10 h, and cooled down to room temperature at a rate of 10 K h^{-1}. Serendipitously, yellow crystals of S_4N_4[60–62] (**10**) were obtained as layered, tetragonal prisms of several 100 μm length, crystallising on the inner surface of the upper half of the ampoule (Fig. S75†); in addition, colourless single-crystals of α-$Sr(NH_2SO_3)_2$ (**8**) embedded in a micro-crystalline powder of $SrSO_4$ were found at the bottom of the ampoule. Heating $Ca(NH_2SO_3)_2$, similarly prepared from **3** or **9** under the same conditions, also lead to the crystallisation of **10**, though neither crystals of sufficient size for single-crystal XRD of $Ca(NH_2SO_3)_2$ were obtained nor any indication for polymorphism was encountered. Heating the same starting materials in an open system with the same temperature program resulted in complete decomposition to the corresponding sulfates in the case of $Sr(NH_2SO_3)_2$ and $Ba(NH_2SO_3)_2$ while $Ca(NH_2SO_3)_2$ decomposed to $(NH_4)_2Ca_2(SO_4)_3$.[63]

2.2 Crystal structure determination

Suited single-crystals were picked under a polarising light microscope and mounted on a MiTeGen MicroMount (compounds **1**–**9**) respectively fused in a Lindemann-glass capillary (**10**). The single-crystal X-ray diffraction data of **1**–**10** were collected using a Bruker D8 Venture diffractometer using Mo-K_α radiation (λ = 0.71073 Å) from an Incoatec Microfocus Source and a Photon II CMOS detector. Absorption correction was performed *via* the multi-scan method with the SADABS program[64] within the APEX 3 suite.[65] The atomic positions of all but hydrogen atoms were found by Direct Methods with SHELXS[66] and refined with anisotropic displacement parameters by full-matrix least-squares refinement against F^2 with SHELXL.[67] Hydrogen positions were determined using a riding model and the N–H distance was fixed at 0.99 Å with a standard deviation of 0.01. The specifics of the crystallographic studies are summarised in Table S6 (ESI†).

2.3 Powder X-Ray diffraction

The powder X-ray diffraction patterns were recorded using a Seifert 3003 TT diffractometer at room temperature in Bragg–Brentano geometry using Cu-K_α radiation, a GE METEOR 1D line detector and a nickel filter to suppress K_β radiation (the X-ray tube was operated at 40 kV and 40 mA, a scan range of 5–80°, an increment of 0.02°, scans per data point of 40, and an integration time of 100 s/°). For temperature-programmed

XRD (TP-XRD), a powdered sample was filled into a silica-glass Hilgenberg sample tube (0.3 mm outer diameter) and the TP-XRD patterns were recorded in the range of 30 °C to 360 °C (steps of 30 °C at a heating rate of 0.1 K min^{-1}) using a Bruker D8 Advance diffractometer in transmission geometry using Cu-K$_\alpha$ radiation and a LynxEye 1-D detector (X-ray tube was operated at 40 kV and 40 mA, a scan range of 5–80°, an increment of 0.02°, and an acquisition time of 1 s per step).

2.4 FT-IR, Raman and UV/vis spectroscopy

The infrared spectra were recorded at room temperature using a Bruker EQUINOX 55 FT-IR spectrometer using a Platinum ATR device (scan range: 400–4000 cm^{-1}, resolution: 4 cm^{-1}, 32 scans per sample). The Raman spectra were measured using a grating spectrometer (Acton, SP-2356) equipped with a CCD detector (Pixis 256E). The Raman spectra were collected for 100 s in a frequency range of 60–4100 cm^{-1} using a Nd:YAG laser with a wavelength of 532.35 nm and a power of 2 mW. The set-up is described in more detail in a study by Bayarjargal et al.[68] The UV/vis spectrum was recorded as a diffuse reflection spectrum at room temperature using a Varian Cary 300 Scan UV/Vis spectrophotometer using an Ulbricht sphere detector and a deuterium lamp/mercury lamp light source (a scan range of 200–800 nm, increment of 1 nm, and scan-rate of 600 nm min^{-1}).

2.5 SHG measurements

Second harmonic generation (SHG) measurements were performed on powdered samples. The powder SHG method was developed by Kurtz and Perry.[69] This method is commonly used as a first step to estimate the nonlinear optical properties of new materials or to detect the absence of an inversion center in crystalline structures. A Q-switched Nd:YAG laser (1064 nm, 5–6 ns, 2 kHz) was used for the generation of the fundamental pump wave. The fundamental infrared light was separated using a harmonic separator, a short-pass filter, and an interference filter from the generated second harmonic (532 nm). The generated SHG signal was collected with a photomultiplier and an oscilloscope from ten different areas of the sample. On each position, 64 pulses were measured and averaged. The measured intensities were corrected using background signals from the laser pulses. The SHG measurements were performed under ambient conditions in transmission geometry. Al$_2$O$_3$, quartz and KH$_2$PO$_4$ (KDP) were used as the reference materials.

2.6 Thermal analysis

Thermogravimetric analyses were performed using a NETZSCH STA 409 PC Luxx thermobalance under a nitrogen atmosphere (flow: 70 ml min^{-1}) in alumina crucibles with an initial isothermal segment at room temperature for 5 min, a heating ramp with a rate of 5 K min^{-1} to 1000 °C, and another isothermal segment at this temperature before cooldown. The isothermal decomposition of the tetrahydrate **5** in a dry inert gas stream was studied by transferring a large single-crystal directly from its mother liquid to the thermobalance. It was covered with a few drops of mother liquid to ensure that dehydration did not start before the weight could be monitored reliably. Then the apparatus was closed immediately and the measurement of the weight as a function of time was started.

2.7 DFT calculations

First-principles calculations were carried out within the framework of density functional theory (DFT)[70] by employing the Perdew–Burke–Ernzerhof (PBE) exchange–correlation function[71] and the plane wave/pseudopotential approach implemented in the CASTEP37 simulation package. "On the fly" norm-conserving pseudopotentials generated using the descriptors in the CASTEP database were employed in conjunction with plane waves up to a kinetic energy cutoff of 1020 eV. The accuracy of the pseudopotentials is well-established.[72] A Monkhorst–Pack[73] grid was used for Brillouin-zone integrations with a distance of <0.023 Å^{-1} between grid points. The convergence criteria included an energy change of $<5 \times 10^{-6}$ eV per atom for scf-cycles, a maximal force of <0.008 eV Å^{-1}, and a maximal component of the stress tensor of <0.02 GPa. Dispersion forces were approximated by the Tkatchenko–Scheffler[74] correction scheme. The phonon frequencies were obtained from the density functional perturbation theory (DFPT) calculations. Raman intensities were computed using DFPT by following the "$2n + 1$" theorem approach.[75]

3. Results and discussion

3.1. Crystal structure description

Mg(NH$_2$SO$_3$)$_2$·4H$_2$O (compound **1**) crystallises isotypically with Mn(NH$_2$SO$_3$)$_2$·4H$_2$O[43] (space group $P2_1/c$, no. 14) as depicted in Fig. 1a. The structure features slightly distorted, non-condensed MgO$_6$ octahedra with apical axes oriented roughly along [11$\bar{1}$]. These are centred by Mg^{2+} ions situated at the
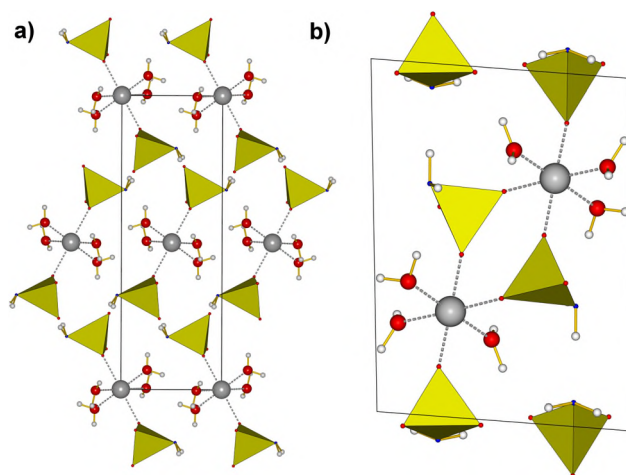
Fig. 1 The unit cells of (a) Mg(NH$_2$SO$_3$)$_2$·4H$_2$O (**1**) and (b) Mg (NH$_2$SO$_3$)$_2$·3H$_2$O (**2**) viewed along [100] (H atoms in white, N atoms in blue, O atoms in red, SO$_3$N tetrahedra in yellow, Mg atoms in grey and covalent bonds as yellow sticks).

origin and coordinated by four oxygen atoms of the crystal water molecules (O_w) at the equatorial positions and by two oxygen atoms of the tetrahedral amidosulphate anions $[NH_2SO_3]^-$ (O_s) at the apical positions (Fig. S1†). The averaged interatomic distances (Table S1†) of the Mg–O (2.06 Å), S–O (1.45 Å) and S–N interactions (1.65 Å) show typical values[43] and correspond reasonably well with the sum of the respective ionic radii.[76] The resulting $Mg(NH_2SO_3)_2(H_2O)_4$ moieties are held together by hydrogen bonds (Table S2†) and arranged in primitively packed layers within the (110) plane with an inclination angle of about 117° between the apical O–Mg–O axis and the layer plane (Fig. S2†). The neighbouring layers feature antiparallel (inclination angle of 117°) displaced octahedra, resulting in an AB stacking of layers (Fig. S3†). The hydrogen bonding pattern within a layer features O–H···O_w, O–H···O_s and O–H···N interactions (Fig. S2†). A three-dimensional framework structure is achieved by means of O–H···O_w as well as N–H···N bonds between the neighbouring layers (Fig. S3†).

$Mg(NH_2SO_3)_2·3H_2O$ (compound **2**) introduces a new structure type (space group $P\bar{1}$, no. 2) as depicted in Fig. 1b. The structure features slightly distorted MgO_6 octahedra with apical axes oriented roughly along [11$\bar{1}$], centred by Mg^{2+} ions coordinated by three oxygen atoms of crystal water molecules O_w and three oxygen atoms belonging to tetrahedral amidosulphate anions O_s (Fig. S4†). The averaged interatomic distances (Table S1†) of the Mg–O (2.06 Å), S–O (1.45 Å) and S–N (1.65 Å) show typical values[43] and correspond reasonably well with the sum of the ionic radii.[76] In contrast to **1**, half of the amidosulfate ions coordinate two adjacent magnesium ions as bridging ligands, thus forming dimeric moieties $[Mg(NH_2SO_3)_2·3H_2O]_2$, while the other half coordinates only a single Mg^{2+} cation (Fig. 1b). These dimers are interconnected by hydrogen bonds (Table S2†) and arranged in a simple tetragonal packing (Fig. S5†). The hydrogen bonding pattern between the molecules features O–H···O_w, O–H···O_s, O–H···N, N–H···O_s as well as N–H···N bonds, resulting in a three-dimensional framework structure.

$Ca(NH_2SO_3)_2·4H_2O$ (compound **3**) crystallises in the space group $C2/c$ (no. 15) as reported by Angerer *et al.*[43] Since our experiments confirm their results (Tables S1 and S2†), we would like to refer the reader to their publication for an explicit structure description, or alternatively to our structure description of the isotypic strontium compound **5** further down.

$Ca(NH_2SO_3)_2·H_2O$ (compound **4**) crystallises in a new structure type (space group $P2_12_12_1$, no. 19) as depicted in Fig. 2a. The structure features distorted CaO_7 pentagonal bipyramids with apical axes oriented roughly along [651] formed by Ca^{2+} ions located at a general position and coordinated by one O_w atom at the equatorial position and O_s atoms at all other positions (Fig. S6 and S7†). The averaged interatomic distances (Table S1†) of the Ca–O (2.38 Å), S–O (1.46 Å) and S–N (1.63 Å) interactions show typical values[43] and correspond reasonably well with the sum of the ionic radii.[76] The four equatorial amidosulphate anions link each CaO_7 bipyramid to six neighbouring bipyramids, forming a hexagonal closely packed layer
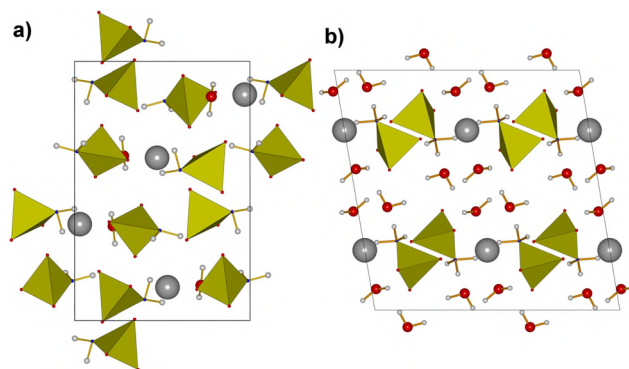

Fig. 2 The unit cells of (a) $Ca(NH_2SO_3)_2·H_2O$ (**4**) viewed along [100] and (b) $Sr(NH_2SO_3)_2·4H_2O$ (**5**) viewed along [010] (H atoms in white, N atoms in blue, O atoms in red, SO_3N tetrahedra in yellow, metal atoms in grey and covalent bonds as yellow sticks).

(Fig. S8†). The apical amidosulphate anions connect the formed layers to a three-dimensional framework structure, featuring a simply AA layered dense packing of CaO_7 bipyramids (Fig. S9†). The hydrogen bonding pattern (Table S2†) can be rationalised starting from a zigzag chain of N–H···N bonds, which connect the amidosulphate anions yielding a 4_1 helix (Fig. S10†). These helices are further interconnected to each other *via* N–H···O_s contacts and to water molecules *via* O–H···O_s, utilising water molecules exclusively as donors (Fig. S11†). As our SHG measurements suggested that **4** might be centrosymmetric (*cf.* Table 1), we tried to solve the structure with SHELXS in the two centrosymmetric minimal supergroups of $P2_12_12_1$, *i.e.* space group types *Pbca* (no. 61) and *Pnma* (no. 62). Furthermore, we transformed our crystal structure model from $P2_12_12_1$ into these space groups with the PowderCell program[77] and tried to refine the resulting structural models. As all of these attempts resulted in a very poor fit to the collected single-crystal data as well as chemically nonsensical interatomic distances and bond angles, we assume that $P2_12_12_1$ is indeed the proper space group type for **4**.

$Sr(NH_2SO_3)_2·4H_2O$ (compound **5**) crystallises isotypically with **3** (space group $C2/c$, no. 15) as depicted in Fig. 2b. The structure features distorted SrO_8 tetragonal antiprisms with the tetragonal faces aligned parallel to {010}, formed by one Sr^{2+} ion located on the edge of the unit cell (Wyckoff position **4e**) and coordinated by four O_w atoms and four O_s atoms (Fig. S12 to S14†). The averaged interatomic distances (Table S1†) of the

Table 1 Observed SHG intensities of the powdered samples of **4**, **7** and **9** relative to quartz

Sample	SHG intensity/counts	I_{SHG}/I_{quartz}
KDP	1608(255)	16.54
Quartz	97(34)	1
Al_2O_3	3(3)	0.03
$Ca(NH_2SO_3)_2·H_2O$ (**4**)	4(3)	0.04
β-$Sr(NH_2SO_3)_2$ (**7**)	167(67)	1.72
$Ba(NH_2SO_3)_2$ (**9**)	1032(392)	10.61

Sr–O (2.58 Å), S–O (1.45 Å) and S–N (1.63 Å) show typical values[43] and correspond reasonably well with the sum of the ionic radii.[76] Each SrO$_8$ antiprism is connected *via* four amidosulphate anions to four neighbouring ones, forming layers parallel to the (001) plane (Fig. S14†). Three maxima in the residual electron density were found by Fourier difference analysis around the nitrogen atom at suitable distances and angles. These were therefore refined as partially occupied hydrogen positions (Fig. S13†). The resulting hydrogen bonding pattern (Table S2†) interconnects the polyhedra within the layers further *via* N–H⋯N, N–H⋯O$_w$ as well as N–H⋯O$_s$ bonds (Fig. S15†). In particular, O–H⋯O$_w$ and O–H⋯O$_s$ connect the neighbouring layers to form a three-dimensional framework structure *via* AB stacking.

Sr(NH$_2$SO$_3$)$_2$·H$_2$O (compound **6**) crystallises in its own structure type (space group $P2_1/c$, no. 14) as depicted in Fig. 3a. The structure features distorted SrO$_8$ tetragonal antiprisms with tetragonal faces aligned parallel to [112] formed by Sr^{2+} located at a general position and coordinated by one O$_w$ atom and seven O$_s$ atoms (Fig. S16 and S17†). The averaged interatomic distances (Table S1†) of the Sr–O (2.61 Å), S–O (1.45 Å) and S–N (1.63 Å) interactions show typical values[43] and correspond well with the sum of the ionic radii.[76] Two neighbouring antiprisms are condensed into dimers by edge-sharing *via* two common O$_s$ atoms (Fig. S16†) and forming closely packed layers of dimers parallel to the (001) plane *via* bridging by two amidosulphate anions to each adjacent dimer (Fig. S18†). A three-dimensional framework structure is obtained by further condensation of the dimer layers *via* bridging amidosulphate anions, yielding an AB stacking of closely packed layers. The hydrogen bonding pattern (Table S2†) can be rationalised starting from a zigzag chain of N–H⋯N bonds (Fig. S19†), which connect amidosulphate anions giving a 4$_1$ helix. These helices are further interconnected to each other *via* N–H⋯O$_s$ bonds and to water molecules *via* O–H⋯O$_s$ as well as

N–H⋯O$_w$ (Fig. S18 andS19†), in contrast to the structure of **4** which does not feature O–H⋯O$_s$ bonds.

β-Sr(NH$_2$SO$_3$)$_2$ (compound **7**) denotes the first modification of Sr(NH$_2$SO$_3$)$_2$, crystallising in its own structure type (space group Pc, no. 7) as depicted in Fig. 3b. The structure features distorted SrO$_8$ tetragonal antiprisms with the tetragonal face aligned parallel to (111), formed by Sr^{2+} ions located at a general position and coordinated by eight O$_s$ atoms (Fig. S20 and S21†). The averaged interatomic distances (Table S1†) of the Sr–O (2.60 Å), S–O (1.46 Å) and S–N (1.62 Å) interactions show typical values[43] and correspond well with the sum of the ionic radii.[76] Of the seven ligating amidosulphate anions one acts as a bidentate ligand, coordinating two oxygen atoms. The SrO$_8$ antiprisms are condensed *via* edge-sharing to zigzag chains parallel to [001] (Fig. S22†), packed in a simple tetragonal rod packing (Fig. S23†). By bridging amidosulphate anions within as well as between the zigzag chains, a three-dimensional framework structure is adopted. Four maxima were found in residual electron density by Fourier difference analysis around the nitrogen atom at suitable distances and angles, and the occupation fixed to 0.5 for all positions as a free occupational refinement failed (Fig. S20 and S24†). The hydrogen bonds (Table S2†) are situated in the voids between the SrO$_8$ chains, further interconnecting the neighbouring chains *via* strong N–H⋯N bonds and intermolecular N–H⋯O$_s$ bonds. In contrast to the crystal structures of **1** to **6**, additional intramolecular N–H⋯O$_s$ are also present.

α-Sr(NH$_2$SO$_3$)$_2$ (compound **8**) denotes the second modification of Sr(NH$_2$SO$_3$)$_2$, crystallising in its own structure type (space group $P2_1$, no. 4) as depicted in Fig. 4a. The structure features distorted SrO$_8$N capped tetragonal antiprisms with the tetragonal face aligned parallel to (120), formed by Sr^{2+} located at a general position and coordinated by one nitrogen atom and eight O$_s$ atoms (Fig. S25 and S26†). The averaged interatomic distances (Table S1†) of the Sr–O/N (2.68 Å), S–O (1.46 Å) and S–N (1.62 Å) interactions show typical values[43]
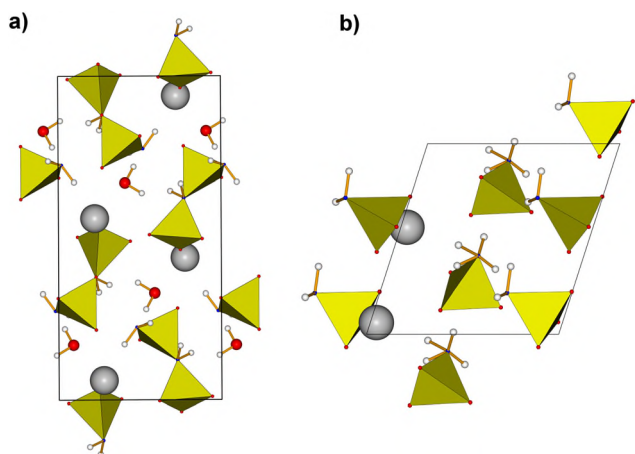

Fig. 3 The unit cells of (a) Sr(NH$_2$SO$_3$)$_2$·H$_2$O (**6**) viewed along [100] and (b) β-Sr(NH$_2$ SO$_3$)$_2$ (**7**) viewed along [010] (H atoms in white, N atoms in blue, O atoms in red, SO$_3$N tetrahedra in yellow, Sr atoms in grey and covalent bonds as yellow sticks).

Fig. 4 The unit cells of (a) α-Sr(NH$_2$ SO$_3$)$_2$ (**8**) and (b) Ba(NH$_2$SO$_3$)$_2$ (**9**) both viewed along [001] (H atoms in white, N atoms in blue, O atoms in red, SO$_3$N tetrahedra in yellow, metal atoms in grey and covalent bonds as yellow sticks).
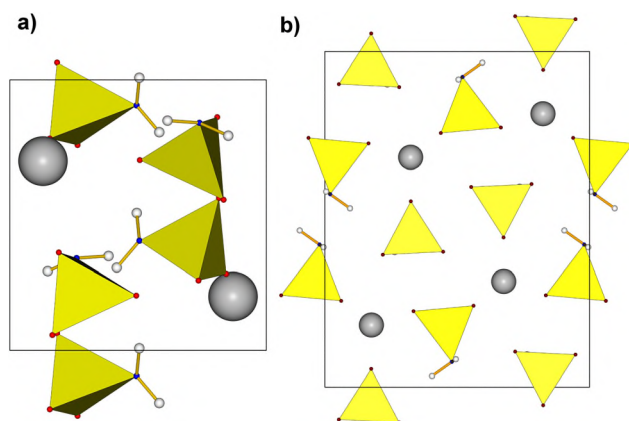
and correspond well with the sum of the ionic radii.[76] Of the eight ligating amidosulphate anions, two act as bidentate ligands, coordinated by both nitrogen and oxygen two oxygen atoms, respectively. The SrO_8N polyhedra are condensed *via* edge-sharing to zigzag chains parallel to [010] (Fig. S27†), packed in a simple tetragonal rod packing (Fig. S28†). By bridging amidosulphate anions within as well as between the zigzag chains, a three-dimensional framework structure is adopted. The hydrogen bonds (Table S2†) are situated in the voids between the SrO_8N chains, further interconnecting the neighbouring chains *via* strong N–H⋯N bonds and intermolecular N–H⋯O_s bonds (Fig. S29†). As for (7), additional intramolecular N–H⋯O_s bonds are present.

$Ba(NH_2SO_3)_2$ (compound 9) crystallises in the space group $Pna2_1$ (no. 33), and all heavy atom positions were found as reported by Manickkavachagam *et al.*[42] As the published crystal structure was reported to be only preliminary and did not include the anisotropic displacement parameters or hydrogen positions, we would like to give a full discussion of our completely refined solution (Fig. 4b). The structure features distorted $BaO_{10}N$ augmented sphenocoronae with the tetragonal face aligned parallel to (791) formed by Ba^{2+} located at a general position and coordinated by one nitrogen atom and ten O_s atoms (Fig. S30 and S31†). The averaged interatomic distances (Table S1†) of the Ba–O/N (2.96 Å), S–O (1.45 Å) and S–N (1.63 Å) interactions show typical values[43] and correspond well with the sum of the ionic radii.[76] Of the eleven ligating amidosulphate anions, three act as bidentate ligands: one is coordinated by both nitrogen and oxygen, while the other two are coordinated solely by oxygen atoms. The $BaO_{10}N$ polyhedra are condensed *via* face-sharing to chains parallel to [001] (Fig. S32†), which are further condensed *via* corner-sharing with neighbouring chains to form layers parallel to (010). By bridging amidosulphate anions within as well as between the layers, a three-dimensional framework structure is adopted *via* AB stacking (Fig. S33†). The hydrogen bonding pattern (Table S2†) features a zigzag chain of N–H⋯N bonds, with a 2_1 helical arrangement of the corresponding amidosulphate groups, and intermolecular N–H⋯O_s, both interconnecting the neighbouring layers (Fig. S34†). As for 7 and 8, additional intramolecular N–H⋯O_s are present.

In order to discriminate between the static and dynamic disorders of the hydrogen atoms around nitrogen as a possible origin for the absence of splitting of the NH_2 stretching vibrations in the IR and Raman spectra discussed below, a set of single-crystal XRD studies of 9 were conducted by varying temperatures along 200 K, 300 K, 400 K and 500 K. The specifics of the temperature-programmed crystallographic studies are given in Table S3 (ESI†). As the measured data neither showed maxima in the residual electron density around nitrogen that are intense enough to justify refinement with a disordered structural model nor any striking temperature dependence regarding the height and location of these maxima could be observed within the studied temperature range, we assume an ordered description of the NH_2 group to be correct within the precision of our experiments.

S_4N_4 (10) crystallizes in the space group $P2_1/n$ (no. 14) in excellent agreement with previous structure elucidations.[78] As our experiments fully confirm their findings, we would like to refer the reader to the corresponding publications for a concise structure description and simply provide a tabular summary of our single-crystal study in the ESI (Table S4†).

3.2. Powder X-ray diffraction

According to the powder X-ray diffraction patterns (XRD, Fig. S35 to S42†), the syntheses yielded phase pure samples for all but the tetrahydrates 3 and 5. As the powder XRD pattern of 3 (Fig. S37†) and the time-dependent room-temperature thermogravimetry of 5 suggest (Fig. S64†), calcium and strontium amidosulphate tetrahydrate crystallites dehydrate rapidly in air after being removed from their mother liquor. In the latter case, this occurs apparently too fast to record a powder XRD pattern showing any reflection belonging to the tetrahydrate. In both cases, all single-crystals arbitrarily selected from the mother liquor and rapidly transferred into a cryogas stream of dry nitrogen in the single-crystal diffractometer consistently proved to be tetrahydrates, such that direct crystallisation of mixed phases from solution seems very unlikely.

The dehydration of 6 at room temperature was studied by aging a freshly synthesised, finely ground sample under air and recording a powder XRD pattern every 24 h (Fig. S43†). After aging the sample for four days, first reflections alluding to 7 emerge in the patterns. The last reflections that can be assigned to 6 disappeared on the sixth day after synthesis, suggesting a much higher stability under ambient conditions than 5 (*cf.* the thermogravimetric study below). TP-XRD between 30 and 360 °C was employed to exemplarily study the thermal decomposition of 7 and scanning for phase transitions to 8 (Fig. 5). At 240 °C, the intensities of all reflections belonging to 7 drastically decrease, while simultaneously broad reflections of $SrSO_4$ emerge. No reflections indicating
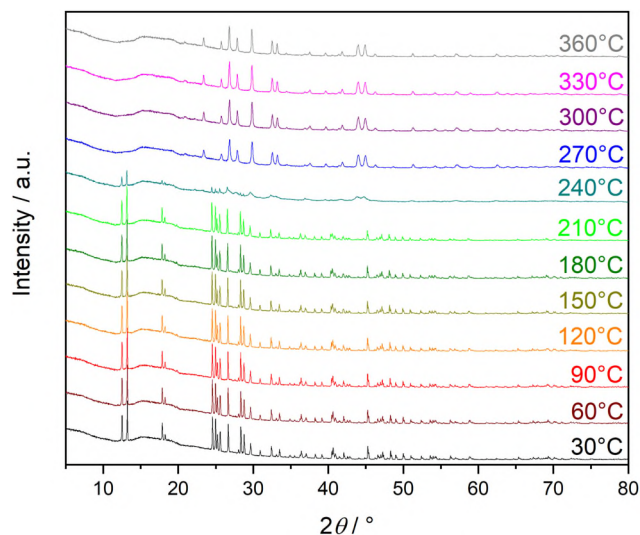

Fig. 5 TP-XRD patterns of β-$Sr(NH_2SO_3)_2$ (7) between 30 and 360 °C.

the presence of **8** are observed at any temperature within the TP-XRD study. In order to study the mechanism of this decomposition, a sample of **7** was heated to the decomposition temperature of 220 °C in a chamber furnace; afterwards, a powder XRD pattern was measured (Fig. S44†). The strongly diminished intensities belonging to **7** together with a notable broad maximum at about 25° suggest the presence of a transient amorphous phase before the crystallisation of $SrSO_4$.

3.3. Infrared and Raman spectroscopy

The room temperature FT-IR spectra of the compounds **1–4**, **6**, **7** and **9** are displayed in Fig. S45 to S51 (ESI†). In addition, room temperature Raman spectra were measured for the non-centrosymmetric compounds **4** and **7** and are shown in Fig. S52–S53.† Temperature programmed Raman spectroscopy has been conducted at 100, 200 and 300 K to study the splitting of vibrational bands at different temperatures (Fig. 6). While the agreement between Raman shifts for frequencies below 1500 cm^{-1} is very satisfactory, there is a systematic blue shift of the DFPT symmetric and asymmetric N–H stretching frequencies in comparison to the experiment. The DFPT calculations correspond to the athermal limit and the harmonic approximation, such that either at temperatures below 100 K there is a yet unknown phase transition or the DFT ground state structure does not adequately describe hydrogen bonding, which would lower the N–H stretching frequencies. The frequencies of all peaks in the FT-IR and Raman spectra are tabulated in Table S5† and assigned to vibrational modes

Fig. 6 Temperature-dependent Raman spectra of $Ba(NH_2SO_3)_2$ (**9**) in comparison to the theoretical data obtained by DFPT calculations. No significant Raman intensities were recorded between 1700 and 3000 cm^{-1}. The two 300 K Raman spectra correspond to the measurements before and after the cooling cycle.

to the best of our knowledge. All compounds show a very good agreement with the IR and Raman studies conducted on other metal amidosulphates[79–82] as well as to the frequencies calculated by DFT.

A clear distinction between H_2O (3700–3400 cm^{-1}), NH_2 (3400–3000 cm^{-1}) and NH_4^+ (3200–2800 cm^{-1}) stretching vibrations can be made, reflecting nicely the differences of relative bond strengths. The bending vibrations of H_2O are found in the range of 1614–1645 cm^{-1}, those of NH_2 at somewhat lower wavenumbers in the regime of 1440–1574 cm^{-1} and those of NH_4^+ at even lower wavenumbers at 1417 cm^{-1}. The antisymmetric and symmetric SO_3 stretching vibrations are found in the range of 1200–1290 cm^{-1} and 1040–1110 cm^{-1}. NH_2 rocking and wagging vibrations can be observed in the range of 1108–1187 cm^{-1} and 856–956 cm^{-1}. S–N vibrations are found in the range of 814–650 cm^{-1}. Antisymmetric and symmetric SO_3 deformation vibrations can be found in the range of 660–546 cm^{-1} and antisymmetric and symmetric SO_3 rocking vibrations can be observed in the range of 416–356 cm^{-1}. The S–N torsion vibrations can be seen in the Raman spectra of (**4**) and (**7**) at 312 cm^{-1} and 300 cm^{-1}. At even lower wavenumbers, external vibrations are found *via* Raman spectroscopy.

From factor group analytical considerations, a splitting of bands is expected for **2**, **4**, **6**, **7**, **8** and **9**, as they exhibit two crystallographically unique $[NH_2SO_3]^-$ anions per unit cell, which is most prominently and easily noticed for the NH_2 stretching modes around 3000 cm^{-1} for **2**, **4**, **7** and **8**. To probe the possible explanations for the absence of splitting for **6** and **9**, a more reliable low temperature Raman study of **9** was performed, strongly confirming the expected splitting of all bands but the NH_2 stretching modes (Fig. 6). As our temperature-programmed single-crystal XRD study shows no indication of dynamic or static disorder of H atoms within the precision of the method, we assume that most likely cooling below 100 K is necessary to observe the splitting of the NH_2 stretching modes.

In order to study the nature of the amorphous phase observed as the reaction intermediate *via* powder XRD during the decomposition of **7**, FT-IR analysis was performed on the sample (Fig. S54†). The NH_4^+ stretching vibrations are clearly seen in the range of 3000 cm to 2600 cm^{-1}, as corroborated by a direct comparison with a sample of $(NH_4)_2SO_4$. As the synthesis temperature of the reaction intermediate is close to the melting point of $(NH_4)_2SO_4$, an amorphous $(NH_4)_2SO_4$ phase seems unlikely. Therefore, we suggest that the observed amorphous phase might be a mixed NH_4^+/Sr^{2+} sulphate, in analogy to crystalline $(NH_4)_2Ca_2(SO_4)_3$ observed during the decomposition of **4**.

3.4. Nonlinear optical properties and UV/vis spectroscopy

To evaluate the non-linear optical properties as well as to prove the absence of inversion symmetry in the corresponding crystal structures, second harmonic generation measurements were performed for the compounds **4**, **7** and **9**. Table 1 shows the intensity of the SHG response of **4**, **7** and **9** in comparison
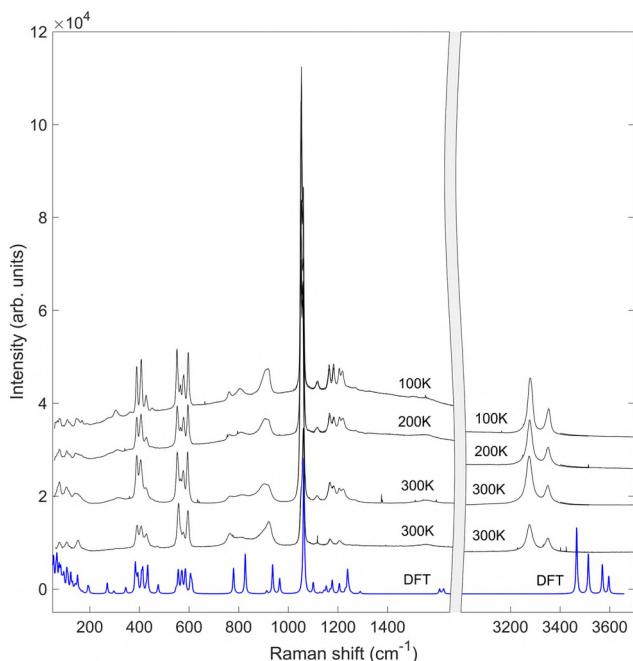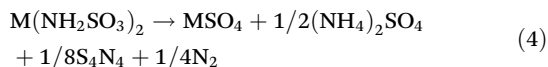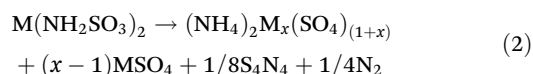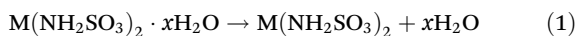
to that of the well-known SHG reference materials quartz and KDP (KH_2PO_4) as well as Al_2O_3 as the centrosymmetric reference. The SHG intensities of these chemically similar compounds vary over about three orders of magnitude; while for **4**, no signal was detected, for **7** about twice the quartz signal and for **9** approximately eleven-fold intensity of quartz was found. As a hypothesis, we suggest that the SHG coefficients of **6** are in the same order of magnitude as quartz. If we also suggest that the SHG coefficients of **6** are comparable with **9**, the strong SHG intensity of **9** can be caused by phase matching conditions.

The UV/vis spectra were recorded for the non-centrosymmetric compounds **4**, **6**, **7** and **9** in order to evaluate their transparency and possible application regime as NLO materials. In addition, the UV/vis spectrum of **2** was recorded to reveal the possible cation effects on the bandgap. As can be seen from the spectra (Fig. S55–S59†), all studied materials showed no absorption in the visible range, with the optical bandgap congruently located at about 380 nm (3.3 eV).

3.5. Thermal analysis

The thermal decomposition of compounds **1** to **7** and **9** was studied *via* thermogravimetry and the obtained thermogravimetric (TG) curves are presented in Fig. S60–S67 (ESI†). The overall decomposition pattern found for all the studied compounds shows a clear separation between the first major decomposition range below 200 °C, featuring the dehydration of crystal water containing compounds to anhydrous metal amidosulphates according to eqn (1) and a second major decomposition range above 200 °C, featuring the decomposition to metal sulphates. Based on our serendipitous discovery of the formation of S_4N_4 as well as our thermogravimetric experiments discussed in the ESI† in detail and the powder XRD patterns of the pyrolysis residues after TG analysis (Fig. S68–S73†), we suggest an overall decomposition scheme according to the following crucial reaction steps:

$$M(NH_2SO_3)_2 \cdot xH_2O \rightarrow M(NH_2SO_3)_2 + xH_2O \quad (1)$$

$$M(NH_2SO_3)_2 \rightarrow (NH_4)_2M_x(SO_4)_{(1+x)} \\ + (x-1)MSO_4 + 1/8S_4N_4 + 1/4N_2 \quad (2)$$

$$(NH_4)_2M_x(SO_4)_{(1+x)} \rightarrow (NH_4)_2SO_4 + xMSO_4 \quad (3)$$

$$M(NH_2SO_3)_2 \rightarrow MSO_4 + 1/2(NH_4)_2SO_4 \\ + 1/8S_4N_4 + 1/4N_2 \quad (4)$$

Decomposition of the amidosulphate anion might either proceed *via* an ammonium mixed cation intermediate (eqn (2) and (3)) or direct yield $(NH_4)_2SO_4$ and MSO_4 (eqn (4)). Mixed cation salts are of *langbeinite* ($(NH_4)_2M_2(SO_4)_3$) type for magnesium and calcium amidosulphates (*cf.* Fig. S70†), while *kalistrontite* type ($(NH_4)_2M(SO_4)_2$) intermediates were not observed. Instead, strontium and barium amidosulphates either directly decompose to the respective sulphate (eqn (4)) or decompose *via* an amorphous ammonium mixed cation phase.

4. Conclusion

In this article, we provided a detailed study of the syntheses, the crystal chemistry and the selected properties of nine members of the alkaline-earth amidosulphate series $M(NH_2SO_3)_2 \cdot xH_2O$ (M = Mg–Ba, x = 0–4). We studied the synthesis conditions, emphasising the rate of dehydration as a pivotal parameter for the obtained phase and crystal sizes. Single-crystal XRD studies were performed to elucidate their crystal structures, which revealed a remarkable variety of packing motifs, including five new non-centrosymmetric crystal structures and one compound, $Sr(NH_2SO_3)_2$, exhibiting polymorphism, both observations in accordance with the general trend observed for metal amidosulphates so far.[27,31,37,49,50] In general, with increasing crystal water content, packings of molecules or dimers are preferred while with decreasing water content salt-like polymeric structures dominate in which all amidosulphate ions bridge coordinated alkaline-earth metal ions to infinite frameworks. Temperature programmed single-crystal XRD was employed to study the static *vs.* dynamic hydrogen disorder for $Ba(NH_2SO_3)_2$ yielding no static disorder down to 200 K. The vibrational properties were studied *via* FT-IR and Raman spectroscopy, and to the best of our knowledge unprecedented in metal amidosulphate chemistry, vibrations were unequivocally assigned to the observed bands based on DFT calculations in combination with a temperature programmed Raman spectroscopical study. The room temperature as well as thermal dehydration of the obtained crystal hydrates and the thermal decomposition of the amidosulphate anions were studied *via* thermogravimetry, TP-XRD and the synthesis of reaction intermediates.

The formation of S_4N_4 during decomposition could be observed and verified by single-crystal XRD, establishing a novel route to sulphur nitrides, unprecedently neither employing sulphur halides nor elemental sulphur as starting materials.[62] The only comparable nitride synthesis mentioned so far throughout the literature is the strongly exothermic reaction of SeO_3 with NH_3 to Se_4N_4, during which an amidoselenic reaction intermediate seems quite likely as $NH_4(NH_2SeO_3)$ can be obtained in similar reactions under mild conditions.[83] Employing our unexpected decomposition reaction for the synthesis of S_4N_4 enables the use of much cheaper starting materials, such as wastewater from boiler scale cleaning solutions. Moreover, our described synthetic approach demands far less elaborate conditions as $M(NH_2SO_3)_2 \cdot xH_2O$ precursors can be handled without an inert atmosphere or dry solvents. This finding will hopefully help to pave the way for the application of some of the many materials that can be synthesised from S_4N_4,[84] like polythiazyl $(SN)_x$, which is of great interest for a range of electrical[85–93] as well as forensic[94,95,96] applications, by providing a method for the *in situ* generation of the explosive starting material S_4N_4 for potential one-pot syntheses.

Conflicts of interest

There are no conflicts to declare.

References

1 H. A. Höppe, *Z. Anorg. Allg. Chem.*, 2005, **631**, 1272–1276.

2 H. A. Höppe, *Solid State Sci.*, 2005, **7**, 1209–1215.

3 H. A. Höppe, M. Daub and M. C. Bröhmer, *Chem. Mater.*, 2007, **19**, 6358–6362.

4 H. A. Höppe, K. Kazmierczak, S. Kacprzak, I. Schellenberg and R. Pöttgen, *Dalton Trans.*, 2011, **40**, 9971–9976.

5 K. Förg and H. A. Höppe, *Dalton Trans.*, 2015, **44**, 19163–19174.

6 K. Förg and H. A. Höppe, *Z. Anorg. Allg. Chem.*, 2015, **641**, 1009–1015.

7 K. Förg and H. A. Höppe, *Z. Anorg. Allg. Chem.*, 2017, **643**, 766–771.

8 M. Daub, H. A. Höppe and H. Hillebrecht, *Z. Anorg. Allg. Chem.*, 2014, **640**, 2914–2921.

9 P. Gross, A. Kirchhain and H. A. Höppe, *Angew. Chem., Int. Ed.*, 2016, **55**, 4353–4355.

10 P. Netzsch, F. Pielnhofer, R. Glaum and H. A. Höppe, *Chem. – Eur. J.*, 2020, **26**, 14745–14753.

11 J. Bruns, H. A. Höppe, M. Daub, H. Hillebrecht and H. Huppertz, *Chem. – Eur. J.*, 2020, **26**, 7966–7980.

12 K. Kazmierczak, J. G. Heck and H. A. Höppe, *Z. Anorg. Allg. Chem.*, 2010, **636**, 409–413.

13 H. A. Höppe, S. W. Scharinger, J. G. Heck, P. Gross, P. Netzsch and K. Kazmierczak, *Solid State Sci.*, 2016, **62**, 50–55.

14 S. G. Jantz, L. van Wüllen, A. Fischer, E. Libowitzky, E. J. Baran, M. Weil and H. A. Höppe, *Eur. J. Inorg. Chem.*, 2016, **2016**, 1121–1128.

15 P. Baumgarten, *Ber. Dtsch. Chem. Ges.*, 1936, **69**, 1929–1937.

16 M. L. Harbaugh and G. A. Peirce, Process for manufacture of sulfamic acid, Du Pont, US2880064A, 1955.

17 G. A. Benson and W. J. Spillane, *Chem. Rev.*, 1980, **80**, 151–186.

18 J. J. Ayo, Jr. and C. M. Knowles, Detergent composition and method of producing same, General Anilin and Film Corp, US2758977A, 1951.

19 W. Douglas and A. Ralph, Flame retardant, water repellent compositions and articles treated therewith, Du Pont, US2723212A, 1953.

20 J.-Y. Winum, A. Scozzafava, J.-L. Montero and C. T. Supuran, *Med. Res. Rev.*, 2005, **25**, 186–228.

21 A. Metzger, ch. Sulfamic Acid, in *Ullmann's Encyclopedia of Industrial Chemistry*, 2000.

22 T. Fukami, M. Seino, K. Nakasone and S. Tahara, *Int. J. Chem.*, 2013, **5**, 1–7.

23 V. Zimmermann, Ph.D. thesis, Justus-Liebig-Universität Gießen, 2017.

24 F. Belaj, C. Kratky, E. Nachbaur and A. Popitsch, *Monatsh. Chem.*, 1987, **118**, 947–954.

25 F. Belaj, C. Kratky, E. Nachbaur and A. Popitsch, *Monatsh. Chem.*, 1987, **118**, 349–354.

26 J. A. Kurzman, G. Jouan, M. Courty, M. R. Palacín, M. Armand and N. Recham, *Solid State Sci.*, 2013, **25**, 28–32.

27 A. Meinhart, E. Haussühl, L. Bohatý and E. Tillmanns, *Z. Kristallogr.*, 2001, **216**, 513–521.

28 C. J. Brown and E. G. Cox, *J. Chem. Soc.*, 1940, 1–10.

29 G. A. Jeffrey and H. P. Stadler, *J. Chem. Soc.*, 1951, 1467–1474.

30 J. Stade, P. Held and L. Bohatý, *Cryst. Res. Technol.*, 2001, **36**, 347–360.

31 E. Haussühl and S. Haussühl, *Z. Kristallogr.*, 1995, **210**, 269–275.

32 R. Manickkavachagam and R. K. Rajam, *Z. Kristallogr.*, 1984, **168**, 179–185.

33 G. W. Cox, T. W. Sabine, V. M. Padmanabhan, N. T. Ban, M. K. Chung and A. J. Surjadi, *Acta Crystallogr.*, 1967, **23**, 578–581.

34 J. Schreuer, *Z. Kristallogr. - New Cryst. Struct.*, 1999, **214**, 305.

35 J. Schreuer, *Z. Kristallogr. - New Cryst. Struct.*, 1999, **214**, 306.

36 J. Schreuer, *Z. Kristallogr. - New Cryst. Struct.*, 1999, **214**, 307–308.

37 T. Fukami, T. Kyan, K. Nakano and R. H. Chen, *Cryst. Res. Technol.*, 2011, **46**, 287–291.

38 V. K. Wadhawan and V. M. Padmanabhan, *Acta Crystallogr., Sect. B: Struct. Crystallogr. Cryst. Chem.*, 1972, **28**, 1903–1907.

39 B. E. Cain and F. A. Kanda, *Z. Kristallogr.*, 1972, **135**, 253–261.

40 J. Schreuer, *Z. Kristallogr. - New Cryst. Struct.*, 1999, **214**, 309–310.

41 F. Belaj, C. Kratky, E. Nachbaur and A. Popitsch, *Monatsh. Chem.*, 1987, **118**, 19–23.

42 R. Manickkavachagam, R. K. Rajaram and K. S. Chandrasekharan, *Curr. Sci.*, 1983, **52**, 420–421.

43 P. Angerer, E. Tillmanns and M. Wildner, *Croat. Chem. Acta*, 1999, **1972**, 295–310.

44 M. S. Wickleder, *Z. Anorg. Allg. Chem.*, 2005, **631**, 2540–2543.

45 J. Toivonen and R. Laitinen, *Acta Crystallogr., Sect. B: Struct. Sci.*, 1984, **40**, 7–9.

46 M. S. Wickleder, *Z. Anorg. Allg. Chem.*, 1999, **625**, 1794–1798.

47 M. S. Wickleder, *J. Alloys Compd.*, 2000, **303–304**, 445–453.

48 M. S. Wickleder, *Z. Kristallogr.*, 2005, **220**, 192–195.

49 G. Tzolova, E. Haussühl and S. Budurov, *Cryst. Res. Technol.*, 1997, **32**, 91–98.

50 S. Budurov, G. Tzolova and L. Bohatý, *Thermochim. Acta*, 1997, **307**, 91–96.

51 G. Varughese, A. S. Kumar and G. Louis, *Phys. B*, 2010, **405**, 1813–1816.

52 S. Budurov and G. Tzolova, *Thermochim. Acta*, 1997, **303**, 101–105.

53 S. G. Jantz, M. Dialer, L. Bayarjargal, B. Winkler, L. van Wüllen, F. Pielnhofer, J. Brgoch, R. Weihrich and H. A. Höppe, *Adv. Opt. Mater.*, 2018, **6**, 1800497.

54 P. Netzsch, M. Hämmer, P. Gross, H. Bariss, T. Block, L. Heletta, R. Pöttgen, J. Bruns, H. Huppertz and H. A. Höppe, *Dalton Trans.*, 2019, **48**, 4387–4397.

55 S. G. Jantz, R. Erdmann, S. Hariyani, J. Brgoch and H. A. Höppe, *Chem. Mater.*, 2020, **32**, 8587–8594.

56 P. Gross and H. Höppe, *Z. Anorg. Allg. Chem.*, 2017, **643**, 1692–1703.

57 P. Gross and H. Höppe, *Chem. Mater.*, 2019, **31**, 8052–8061.

58 P. Gross and H. Höppe, *Z. Anorg. Allg. Chem.*, 2019, **645**, 257–266.

59 P. Gross and H. A. Höppe, *Chem. – Eur. J.*, 2020, **26**, 14366–14376.

60 M. W. Gregory, *J. Pharm. Sci. Accessoires*, 1835, **21**, 315–317.

61 M. W. Gregory, *J. Pharm. Sci. Accessoires*, 1835, **22**, 301–303.

62 T. Chivers, *A Guide to Chalcgen-Nitrogen Chemistry*, World Scientific Publishing, 2005, pp. 85–89.

63 D. Speer and E. Salje, *Phys. Chem. Miner.*, 1986, **13**, 17–24.

64 Bruker, *SADABS*, Bruker AXS Inc., Madison, Wisconsin, USA, 2001.

65 Bruker, *APEX3*, Bruker AXS Inc., Madison, Wisconsin, USA, 2012.

66 G. M. Sheldrick, *Acta Crystallogr., Sect. A: Found. Crystallogr.*, 2008, **64**, 112–122.

67 G. M. Sheldrick, *Acta Crystallogr., Sect. C: Struct. Chem.*, 2015, **71**, 3–8.

68 L. Bayarjargal, C.-J. Fruhner, N. Schrodt and B. Winkler, *Phys. Earth Planet. Inter.*, 2018, **281**, 31–45.

69 S. Kurtz and T. Perry, *J. Appl. Phys.*, 1968, **39**, 3798–3813.

70 P. Hohenberg and W. Kohn, *Phys. Rev.*, 1964, **136**, B864.

71 J. P. Perdew, K. Burke and M. Ernzerhof, *Phys. Rev. Lett.*, 1996, **77**, 3865.

72 S. J. Clark, M. D. Segall, C. J. Pickard, P. J. Hasnip, M. I. J. Probert, K. Refson and M. C. Payne, *Z. Kristallogr.*, 2005, **220**, 567–570.

73 K. Lejaeghere, G. Bihlmayer, T. Björkman, P. Blaha, S. Blügel, V. Blum, D. Caliste, I. E. Castelli, S. J. Clark, A. Dal Corso, S. de Gironcoli, T. Deutsch, J. K. Dewhurst, I. Di Marco, C. Draxl, M. Dułak, O. Eriksson, J. A. Flores-Livas, K. F. Garrity, L. Genovese, P. Giannozzi, M. Giantomassi, S. Goedecker, X. Gonze, O. Grånäs, E. K. U. Gross, A. Gulans, F. Gygi, D. R. Hamann, P. J. Hasnip, N. A. W. Holzwarth, D. Iuşan, D. B. Jochym, F. Jollet, D. Jones, G. Kresse, K. Koepernik, E. Küçükbenli, Y. O. Kvashnin, I. L. M. Locht, S. Lubeck, M. Marsman, N. Marzari, U. Nitzsche, L. Nordström, T. Ozaki, L. Paulatto, C. J. Pickard, W. Poelmans, M. I. J. Probert, K. Refson, M. Richter, G.-M. Rignanese, S. Saha, M. Scheffler, M. Schlipf, K. Schwarz, S. Sharma, F. Tavazza, P. Thunström, A. Tkatchenko, M. Torrent, D. Vanderbilt, M. J. van Setten, V. Van Speybroeck, J. M. Wills, J. R. Yates, G.-X. Zhang and S. Cottenier, *Science*, 2016, **351**, aad3000.

74 A. Tkatchenko and M. Scheffler, *Phys. Rev. Lett.*, 2009, **102**, 073005.

75 K. Miwa, *Phys. Rev. B: Condens. Matter Mater. Phys.*, 2011, **84**, 094304.

76 R. D. Shannon, *Acta Crystallogr., Sect. A: Cryst. Phys., Diffr., Theor. Gen. Crystallogr.*, 1976, **32**, 751–767.

77 W. Kraus and G. Nolze, *J. Appl. Crystallogr.*, 1996, **29**, 301–303.

78 D. Clark, *J. Chem. Soc.*, 1952, 1.

79 P. Muthusubramanian and A. S. Raj, *Can. J. Chem.*, 1982, **61**, 2058–2052.

80 R. S. Katiyar, *Proc. Natl. Acad. Sci., India, Sect. A*, 1965, **62**, 169–175.

81 A. S. Raj and P. Muthusubramanian, *J. Raman Spectrosc.*, 1982, **12**, 24–29.

82 A. M. Vuagnat and E. L. Wagner, *J. Chem. Phys.*, 1957, **26**, 77–82.

83 K. Dostál and J. Krejčí, *Z. Anorg. Allg. Chem.*, 1958, **296**, 29–35.

84 T. Chivers, *A Guide to Chalcgen-Nitrogen Chemistry*, World Scientific Publishing, 2005, pp. 17–30.

85 R. A. Scranton, J. S. Best and J. O. McCaldin, *J. Vac. Sci. Technol.*, 1977, **14**(4), 930–934.

86 M. J. Cohen and J. S. Harris, *Appl. Phys. Lett.*, 1978, **33**, 812–814.

87 R. A. Scranton, *J. Appl. Phys.*, 1977, **48**, 3838–3842.

88 A. E. Thomas, J. Woods and Z. V. Hauptman, *J. Phys. D: Appl. Phys.*, 1983, **16**, 1123–1136.

89 T. Arakawa, M. Kimura and H. Kobayashi, Light-chargeable silver-halogen batteries, Asahi Chemical Industry Co. Ltd., JPS55137671A, 1979.

90 T. Arakawa, H. Kobayashi and K. Takasuka, Schottky barrier-type semiconductor element, Asahi Chemical Industry Co. Ltd., JPS55130181A, 1979.

91 T. Arakawa and M. Ozaki, High-power battery, Asahi Chemical Industry Co. Ltd., JPS5893164A, 1981.

92 R. J. Nowak, C. L. Joyal and D. C. Weber, *J. Electroanal. Chem.*, 1983, **143**, 413–417.

93 N. Radić and H. B. Mark, Jr., *Anal. Chim. Acta*, 1982, **144**, 253–259.

94 P. F. Kelly, R. S. P. King and R. J. Mortimer, *Chem. Commun.*, 2008, 6111–6113.

95 S. M. Bleay, P. F. Kelly and R. S. P. King, *J. Mater. Chem.*, 2010, **20**, 10100–10102.

96 S. M. Bleay, P. F. Kelly, R. S. P. King and S. Thorngate, *Sci. Justice*, 2019, **59**, 606–621.